IEEE Access
Multidisciplinary ⋮ Rapid Review ⋮ Open Access Journal

Received 14 June 2023, accepted 27 June 2023, date of publication 30 June 2023, date of current version 6 July 2023.

Digital Object Identifier 10.1109/ACCESS.2023.3291076

RESEARCH ARTICLE

Fast and Accurate CNN-Based Machine Learning Approach for Microwave Medical Imaging in Cancer Detection

SANDRA COSTANZO[1,2,3,4], (Senior Member, IEEE), ALEXANDRA FLORES[1], (Student Member, IEEE), AND GIOVANNI BUONANNO[1,3], (Member, IEEE)

[1]DIMES, University of Calabria, 87036 Rende, Italy
[2]National Research Council of Italy (CNR)—Institute for Electromagnetic Sensing of the Environment (IREA), 80124 Naples, Italy
[3]Inter-University National Research Center on Interactions between Electromagnetic Fields and Biosystems (ICEmB), 16145 Genoa, Italy
[4]Consorzio Nazionale Interuniversitario per le Telecomunicazioni, 43124 Parma, Italy

Corresponding author: Sandra Costanzo (costanzo@dimes.unical.it)

This work was supported in part by Ministero dell'Università e della Ricerca (MUR), Italy, through the Project PNRR PE8—Conseguenze e sfide dell'invecchiamento "Ageing well in an Ageing Society (Age-IT);" and in part by Programma Operativo Nazionale (PON) Ricerca e Innovazione (2014–2020) through the Project Non-invasive Electromagnetic Green Devices and Methods for Advanced Medical Diagnostics.

ABSTRACT The application and comparison of U-Net convolutional neural network architectures is proposed in this work to guarantee a fast and accurate convergence of inverse scattering problems solved by Born iterative method, even in the presence of strong scatterers. Starting from a preliminary configuration proposed by the authors in some recent papers, two variants are introduced and discussed to significantly reduce the computational cost, while guaranteeing convergence with very high accuracy in the dielectric profiles reconstruction when considering strong scatterers, such as tumors, thus working as a regularization process to mitigate the induced non-linearity. As a further enhancement, a novel approach is introduced which integrates U-Net and Resnet models to realize a segmentation process, thus leading to the effective feature extraction and the accurate identification of anomalies within healthy tissue. Numerical assessments on a variety of breast models including abnormal lesions are discussed to successfully validate the proposed machine learning approach, through the adoption of properly defined evaluation metrics.

INDEX TERMS Inverse scattering problem, machine learning, Born iterative method, convolutional neural networks, breast cancer, tumor segmentation.

I. INTRODUCTION

Inverse Scattering Problems (ISPs) arise in microwave imaging procedures to identify, from the measured scattered field, the size, position, shape, and constitutive properties of a target, including its relative permittivity and conductivity. They give the basic mathematical formulation usually required in many physical contexts, such as biomedical imaging [1], through-the-wall imaging [2], remote sensing [3] and geophysics [4]. Nonlinearity and ill-posedness remain significant challenges in ISPs. In general, conventional ISP approaches extract unknown parameters using nonlinear optimization with regularization terms [5]. The distorted Born iterative method (DBIM) [6], the contrast source inversion (CSI) approach [7], [8], and the subspace optimization method (SOM) [9] give some examples of typical nonlinear ISP methods. These approaches are significantly powerful to solve ISPs in a wide variety of applications, but they still demand for large computational costs, and the image quality can be drastically deteriorated in those cases dealing with severe nonlinearities and strong scatterers.

To address the above issues of high computational cost and lower reconstruction accuracy, machine learning-based inversion algorithms [10], [11] can be applied. In particular,

The associate editor coordinating the review of this manuscript and approving it for publication was Larbi Boubchir.

deep convolutional neural networks (CNN) have revealed to provide a promising method for solving inverse issues in recent years, due to the increasing availability of very big datasets, as well as the associated growth in the computational capacity [12], [13]. As a matter of fact, CNN-based techniques have been successfully adopted for X-ray computed tomography [14], computational optical imaging [15] and magnetic resonance imaging [16].

Establishing a correlation between a conventional iterative solution approach for inverse electromagnetic scattering with a deep convolutional neural network (DCNN) is feasible. Specifically, a dielectric imaging technique including CNN assistance is introduced in [17], with the objective to extract the maximum information from magnetic resonance (MR) images, resolve the microwave inverse scattering problem, and produce accurate dielectric images. The study presented in [18] explores the correlation between traditional iterative inverse-scattering algorithms and DNNs to create the DeepNIS network. This network includes three successive CNNs which analyze an image generated by backpropagation (BP) to estimate the dielectric distribution with high precision. Some of these powerful algorithms also adopt traditional CNN architectures, such as U-NET [19], which is based on a fully convolutional network model [20], where the fundamental objective is to extend a conventional contracting network by adding successive layers, with the aim of exchanging pooling operators for up-sampling operators in each succeeding layer. The authors of [21] have introduced the framework LeNet-5, a relatively simple design. Different versions of this network have been evaluated on the standard MNIST database, and this network performed exceptionally well. AlexNet, another classic network, was introduced in [22], where the authors evaluated the network on the ImageNet dataset, likewise demonstrating outstanding performance. ResNet, an enhanced convnet architecture, was presented in [23]. The ImageNet database was used to test the performance of this residual network, which achieved positive results. Recursive neural network topologies [24], [25] influenced by proximal gradient algorithms, which alternate between CNN blocks and steeper descent steps, have been also developed.

These architectures have revealed superior performance in a variety of circumstances; however, training neural networks can be computationally expensive, as well as requiring large amounts of data to obtain the desired accuracy. To implement an acceptable solution, giving a balanced compromise in terms of computational load and accuracy degree, it is essential to analyze the following factors: selecting a potentially effective ''optimal'' network architecture, choosing the optimal network hyper-parameters, identifying the amount of data needed for training, and checking to see if training can be accomplished within the required cost.

The framework proposed in this work combines the Born Iterative method (BIM) with a quadratic programming approach to tackle the inverse problem and exploit the capabilities of CNNs for deep learning-based image reconstruction and segmentation. The main focus is to examine the performance of three architectures incorporating U-Net for the reconstruction of breast dielectric profiles and U-Net+Resnet18 to perform tumor segmentation. The first inspiring architecture for reconstruction is originally introduced in our preliminary papers [26], [27], [28], and the other two are specifically conceived to significantly reduce the computational cost, by leaving unchanged the reconstruction accuracy. The purpose is to choose the best CNN model for breast phantom reconstruction and tumor segmentation. To assess the proposed architectures, we examine the reconstruction of three breast models using data from the available repository of the University of Wisconsin Computational Electromagnetics Laboratory (UWCEM) [29]. The analysis for the reconstruction and segmentation is concentrated on the estimation of the execution time initially for the quadratic BIM, followed by the estimation of the training time for each epoch, the total time used by the entire proposed (approach) and the reconstruction time after training.

The remaining of the paper is organized as follows. Section II describes the formulation of the ISP and the BIM, the different characteristics of the three types of proposed networks, and the segmentation procedure. The comparison and the evaluation of results achieved with the different network architectures are discussed in Section III. Finally, conclusions are outlined in Section IV.

II. METHODOLOGY

A 2-*D* transverse-magnetic scenario is considered in the present work [10]. In particular, N_i line sources illuminate a domain of interest D, where electromagnetic waves interact with scatterers. The scattered field is then collected at surface S by N_r antennas. (see scenario at the left side of Fig. 1).

A BIM strategy is considered which optimizes the inverse subproblem using Quadratic Programming approach [30], making it possible to employ an exact methodology with an appropriate mechanism to enforce a specific type of *a priori* information, as the upper and lower bounds of the range of contrast values for the object to be reconstructed. In the adopted method, the optimization is performed by minimizing the residual error between the measured scattered field $\widetilde{E_m^s}$ and the computed scattered field E_m^s [26], [27], [28], namely:

$$\min_{\{\chi_n\}} \sum_{m=1}^{M} \left| \widetilde{E_m^s} - \sum_{n=1}^{N} g_{mn}\, \chi_n\, E_n^t \right|^2 \qquad \chi_n \in \mathbb{C}, \quad n = 1, \ldots, N \tag{1}$$

where:

$$g_{mn} = -\frac{j}{2}\, \pi\, k_b\, a_n\, J_1(k_b\, a_n)\, H_0^{(2)}(k_b\, |r_m - r_n|) \tag{2}$$

is the discretized version of the Green's function, and:

- $a_n = \sqrt{\Delta x \Delta y / \pi}$;

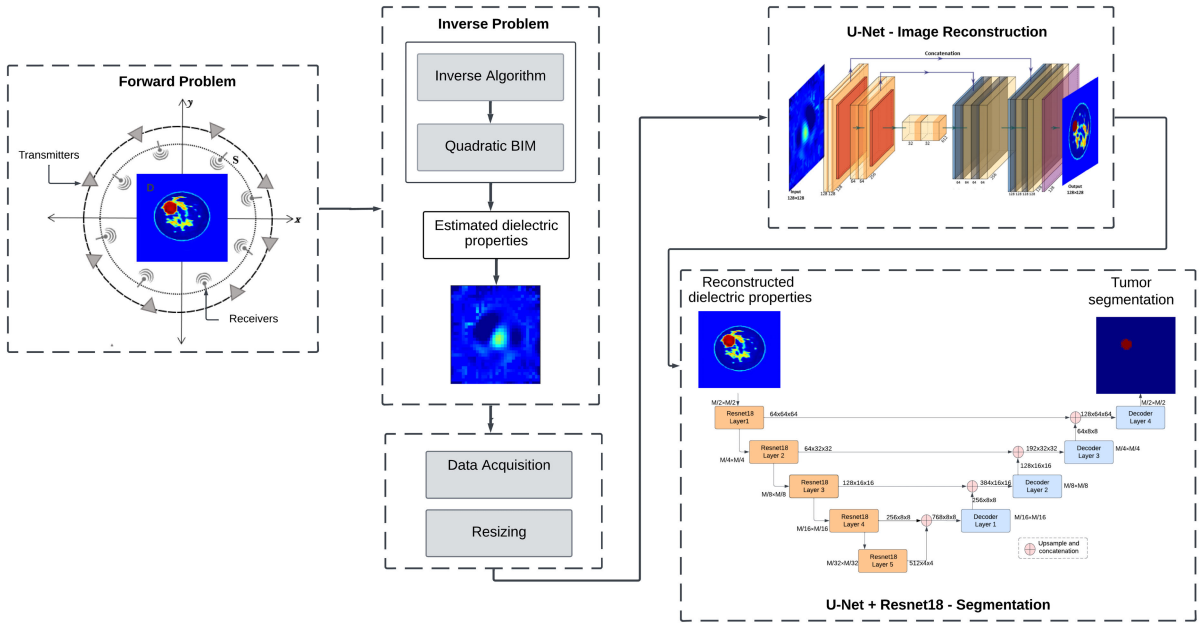

FIGURE 1. General framework of the proposed methodology.

- r_n is the vector position of the n-*th* pixel in D;
- $J_1(\cdot)$ is the Bessel function of the first kind;
- $H_0^{(2)}(\cdot)$ is the Hankel function of the second kind of order 0;
- $k_b = \omega\sqrt{\varepsilon_b \mu_0}$ is the wavenumber of the homogeneous medium background with relative permittivity ε_b;
- χ_n is the contrast value at r_n, which is defined as: $\chi(r) = \frac{\varepsilon_r(r)}{\varepsilon_{r_b}} - 1 - j\frac{(\sigma(r)-\sigma_b)}{\omega\varepsilon_b}$
- E_n^t is the total electric field at position r_n.

This section describes the procedure performed to achieve the highest detection accuracy, with minimum computational cost, to detect breast tumors using microwave tomography, even in the presence of strong scatterers ideally preventing the Born approximation [31]. The ISP is initially solved using the quadratic BIM described above, and then, to enhance the reconstruction, a Machine Learning model is applied, by considering three different U-Net architectures, with the final end to reduce the overall computational cost. Each U-Net architecture adopted to reconstruct the breast images also includes a second U-Net model with a Resnet backbone, which is created and trained to carry out the tumor segmentation task. The general framework of the proposed methodology is shown in Fig. 1.

A. INVERSE SCATTERING PROBLEM

The scattering process recovers the spatial distribution of dielectric parameters. This procedure is executed by employing three MRI (Magnetic Resonance Imaging) heterogeneous numerical breast phantoms (Class 1, Class 2, Class 3) from the available Repository of the University of Wisconsin Computational Electromagnetics Laboratory(UWCEM) [29]. This online repository contains a collection of anatomically realistic MRI-based numerical breast phantoms which incorporate the realistic dispersive dielectric characteristics of normal breast tissue between 0.5 and 20 GHz. In the present work, a single 1GHz frequency is adopted. BIM with quadratic programming is applied to solve the forward problem with 11 transmitting antennas and 11 receiving antennas, as shown in Fig. 1. The diameter of the acquisition circle is equal to 20 cm. The background medium permittivity is fixed to 10, with zero conductivity (ideal lossless medium), while breast phantoms have a realistic range of permittivity between a minimum of 2.5 and a maximum of 67. As demonstrated in our previous works [26], [27], [28], it is not possible to obtain a sufficient and accurate reconstruction using the quadratic BIM model only. In order to overcome this issue, a data collection containing simulations of the various breast phantoms is created by solving the ISP. Therefore, the technique based on the BIM model and quadratic programming seeks to obtain as many samples as possible, including the permittivity and conductivity distribution of the breast models. Each sample consists of a permittivity and conductivity distribution vector with a 128×128 element resolution. A total of 1500 samples of three types of phantoms (from the least dense to the most dense one) are simulated by introducing tumors in random positions inside the breast tissue with diameters between 0.6 cm and 1.6 cm. The distribution and quantity of samples are depicted in Fig. 2. Subsequently, all samples are separated into a training set and a validation set, to be trained in the convolutional neural network stage.

B. CONVOLUTIONAL NEURAL NETWORK

As shown in Fig. 1, a Machine Learning model is performed to overcome the limitations of BIM, thus enhancing

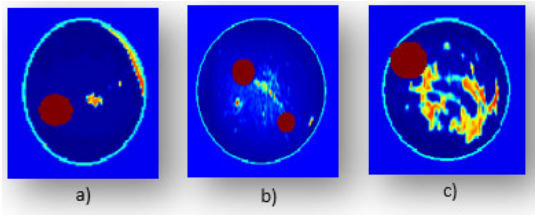

FIGURE 2. Breast phantoms and number of different samples. a)Class 1: 500 samples, b)Class 2: 500 samples and c)Class 3: 500 samples.

the reconstruction of dielectric profiles. In order to accomplish for this, CNN is based on the U-net [19], which is initially created for segmentation. Several specific features of its architecture make it suitable for our goals. For this procedure, images from the breast imaging dataset estimated by the BIM are resized for use as input to the CNN. The strength of the U-Net architecture is related to its ability to identify unclear and jagged discontinuities and boundaries, otherwise strongly difficult to be detected with conventional methods, especially regarding tumor region detection issues. In this paper, three CNN architectures are discussed, namely:

1) The first architecture is introduced in our previously published works [26], [27], [28] and reported in Fig. 3. This network is based on a (CNN) and consists of an encoding and a decoding part. The input image from the network is of size 128 × 128 pixels. The contracting path employs two 3 × 3 convolutional layers with stride 1, containing 128 filters of size 128 × 128; each convolution is followed by batch normalization and rectified linear unit (ReLU). Next, a max pooling operation of 2 × 2 with stride 2 is applied; in this case, the filters are doubled to 256, and the size of the feature maps is reduced to 64 × 64. The lower level consists of two 3 × 3 convolutional layers and a 2 × 2 max pooling layer; consequently, the number of filters is increased to 512, and the size of the feature map is reduced to 32×32. The expansive path can resample the feature maps from the bottom up to recover the original dimensions of the input images, by means of a 2 × 2 up-sampling layer followed by two 3 × 3 convolutions, with batch normalization and rectified linear unit (ReLU). In this instance, the filters are reduced from 256 to 128, and the size of the feature maps is doubled to 64 × 64. The same process is repeated at the next level of the expansive path of the network, yielding 128 filters and a dimension of 128 × 128 pixels. In the expansive path there are also two concatenations with the corresponding feature maps of the contractive path, which allows extracting the most important features of the previous layers and joining them to the current layers. The final layer is a 1 × 1 convolution to map the feature vector to the final prediction.
2) Regarding the second architecture, depicted in Fig. 4, a modification is performed to the previous network. In particular, one convolution level is increased, and the number of filters in each layer is halved from 128 to 64.
3) The third architecture, illustrated in Fig. 5, maintains the same number of network levels as in case 1, but only reducing the number of filters from 128 to 64.

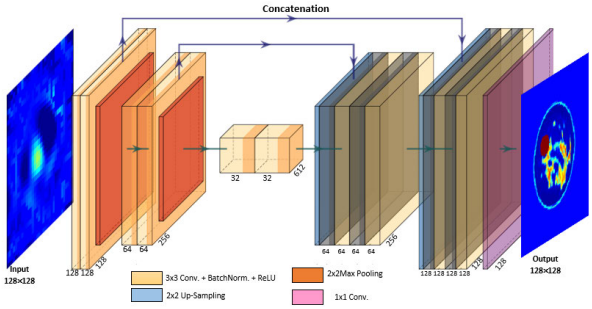

FIGURE 3. Illustration of the U-net architecture 1.

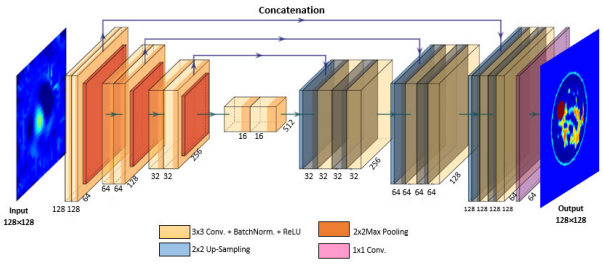

FIGURE 4. Illustration of the U-net architecture 2.

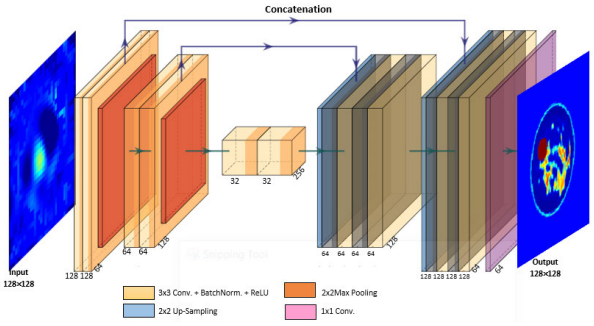

FIGURE 5. Illustration of the U-net architecture 3.

The modifications made in cases 2 and 3 are intended to simplify the architecture and reduce the training computational cost.

1) TRAINING PROCEDURE

As regarding the training stage, 1500 images generated with the quadratic BIM algorithm are adopted. The images estimated by the quadratic BIM are resized from 64 × 64 to 128 × 128 pixels, and they are used as input for the three CNN architectures described in the previous paragraph. The dataset is randomly divided into 80% for training and 20% for network validation. The test set is constructed from data distinct from the training set, 10dB and 20 dB of white

Gaussian noise are also introduced. The test set is used to validate the generalization capability of the model.

C. TUMOR SEGMENTATION

The segmentation process of the images obtained from each U-Net architecture is incorporated into our proposed approach to enhance the precision of breast tumor detection and identification. The segmentation task employs an extended version of the U-Net architecture, which integrates ResNet-18 as a backbone for feature extraction. The dielectric profiles reconstructed in the preceding step are used as input for the network, while the tumor masks represent the output, as depicted in Figure 6. In this case, the ResNet-18 architecture is applied instead of the traditional U-Net encoder path. Specifically, the ResNet-18 [32], [33] model is a convolutional neural network characterized by its deep architecture and residual connections. The structure is composed by 18 layers, which include residual blocks. The utilization of residual connections enables the direct propagation of gradients from subsequent layers to earlier layers, thereby facilitating the learning process of the network and mitigating the issue of fading gradients. The utilization of residual connections within ResNet-18 facilitates the acquisition and retention of pertinent features throughout the encoding procedure. The aforementioned characteristics can be subsequently employed by the decoder path to achieve precise segmentation.

In the following, the individual components of the proposed segmentation network is described in detail.

- Encoder Path (Resnet 18):
  The input to the network is a single-channel image with a dimension of M×M (128 × 128) pixels. The initial layer (Layer 1) includes a convolutional layer with a kernel size of 7 × 7, featuring 64 filters, a stride of 2, and a padding of 3. Batch normalization is implemented on the output of the convolutional layer, followed by the Rectified Linear Unit (ReLU) application as the activation function. Then, a max pooling operation is executed with a kernel size of 3 × 3, a stride of 2, and a padding of 1. ResNet-18 comprises residual blocks, namely layer2, layer3, layer4, and layer5, each encompassing two basic blocks. The basic blocks consist of a pair of 3 × 3 convolutional layers, each with 64, 128, 256, and 512 filters, respectively. The utilization of batch normalization and ReLU activation is implemented after every convolutional layer. The downsampling process is executed within the layer3, layer4, and layer5 blocks through convolutional layers featuring a stride value of 2. In addition, skip connections are established within the downsampling blocks to concatenate feature maps originating from the encoder path to those on the decoder path.
- Decoder Path:
  The part responsible for decoding includes a sequence of three deconvolutional blocks. Each deconvolutional block executes upsampling through the utilization of transpose convolution with a kernel size of 2 × 2 and a stride of 2. Each block also includes a pair of convolutional layers which use a kernel size of 3 × 3. After each convolutional layer, Batch Normalization and ReLU activation functions are implemented.
  The output block executes the final upsampling process by utilizing transpose convolution. The architecture comprises a convolutional layer with a kernel size of 3 × 3 and 64 channels. The convolutional layer is followed by applying Batch Normalization and ReLU activation. The network output is achieved by employing a 1 × 1 convolutional layer which produces two output channels, corresponding to the number of segmentation classes.

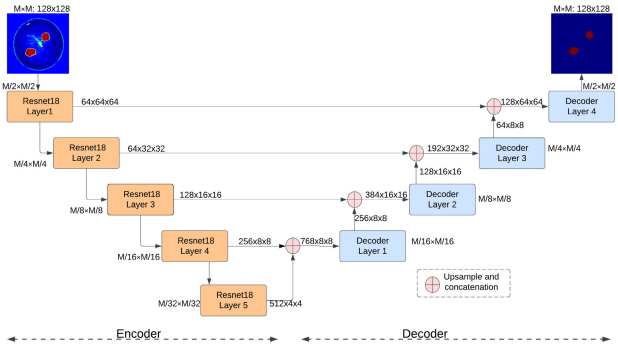

FIGURE 6. U-Net architecture, which incorporates a ResNet18 backbone for tumor segmentation.

The involved network optimization process adopts the loss function Binary cross-entropy (BCE) with logits loss [34]. This function applies the sigmoid activation function to the network outputs, thereby constraining them from 0 to 1. The binary cross entropy function is computed using the following equation:

$$L_{BCE} = -\frac{1}{N}\sum_{i=1}^{N}[p_i \ln \widehat{p_i} + (1-p_i)\ln(1-\widehat{p_i})] \quad (3)$$

where $\widehat{p_i}$ represents the predicted probability of the i-th pixel, and p_i gives the ground-truth value for the same pixel.

III. NUMERICAL RESULTS

In this section, three numerical examples are provided to illustrate the effectiveness of the deep neural network-based inversion and segmentation strategy for breast imaging. The first numerical scenario evaluates the performance of the three proposed U-Net models for reconstructing the dielectric profile and then performing the tumor segmentation task for a sparse breast model (Class 1), the second numerical scenario for a slightly dense breast model (Class 2), and the third numerical scenario for a dense breast model (Class 3). In addition, white Gaussian noise contamination with a signal-to-noise ratio (SNR) equal 10 dB and 20 dB is added to data for the three phantom scenarios, with the aim

TABLE 1. Evaluation metrics performed by the three types of U-Net architecture.

		Quadratic BIM			Quadratic BIM+CNN ($FreeNoise$)			Quadratic BIM+CNN ($10dBNoise$)			Quadratic BIM+CNN ($20dBNoise$)		
		Re[%]	RMSE	R^2	Re[%]	RMSE	R^2	Re[%]	RMSE	R^2	Re[%]	RMSE	R^2
U-Net1	Class1	16.74	5.38	0.27	4.57	2.07	0.89	17.91	5.37	0.44	7.31	2.77	0.84
	Class2	24.49	7.19	0.13	5.92	2.14	0.92	17.37	7.06	0.13	7.39	3.52	0.80
	Class3	26.97	10.16	0.18	3.34	1.27	0.98	15.72	6.09	0.53	7.08	3.38	0.87
	Mean	**22.73**	**7.58**	**0.07**	**4.61**	**1.82**	**0.93**	**17.00**	**6.58**	**0.33**	**7.26**	**3.22**	**0.84**
U-Net2	Class1	16.74	5.38	0.27	3.42	1.53	0.94	15.58	5.08	0.45	7.38	3.00	0.80
	Class2	24.49	7.19	0.13	5.56	1.85	0.93	17.99	7.32	0.02	8.77	3.90	0.73
	Class3	26.97	10.16	0.18	3.13	1.09	0.99	10.04	4.61	0.73	5.47	2.95	0.90
	Mean	**22.73**	**7.58**	**0.07**	**4.04**	**1.49**	**0.95**	**14.54**	**5.67**	**0.40**	**7.21**	**3.28**	**0.81**
U-Net3	Class1	16.74	5.38	0.27	4.87	2.10	0.88	20.62	6.11	0.26	8.51	3.42	0.75
	Class2	24.49	7.19	0.13	7.21	2.42	0.90	18.37	7.19	0.16	8.81	3.78	0.77
	Class3	26.97	10.16	0.18	4.71	1.59	0.97	17.31	6.09	0.55	8.08	3.68	0.85
	Mean	**22.73**	**7.58**	**0.07**	**5.60**	**2.04**	**0.92**	**18.77**	**6.47**	**0.32**	**8.34**	**3.63**	**0.79**

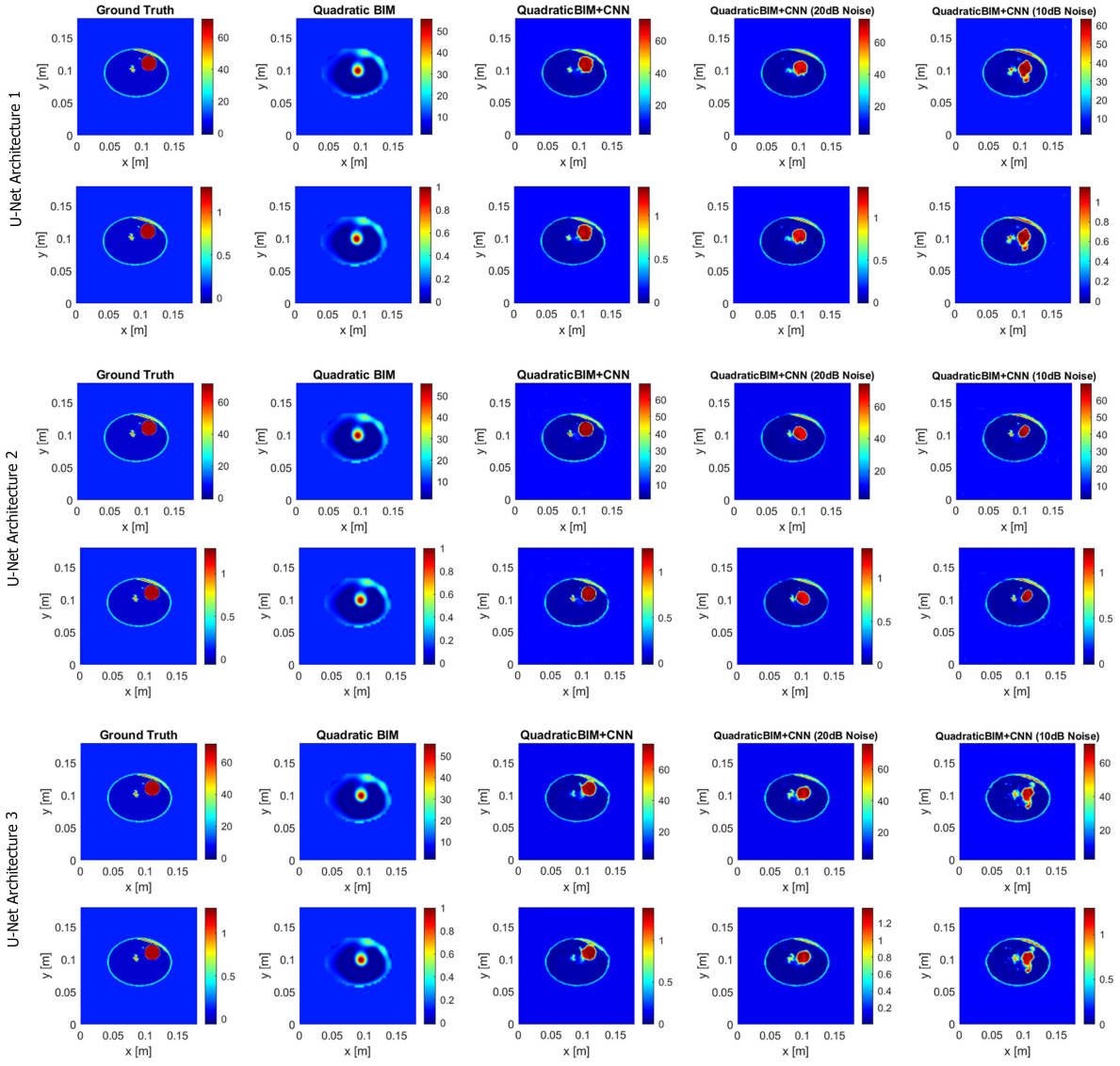

FIGURE 7. Results obtained for the three U-Net architectures - example of Class 1 breast phantom: permittivity (upper) and conductivity (lower).

to assess the reconstruction and segmentation capabilities of the proposed model.

The aim of the reconstruction procedure is to obtain the complete image of the breast including the tumors, for which

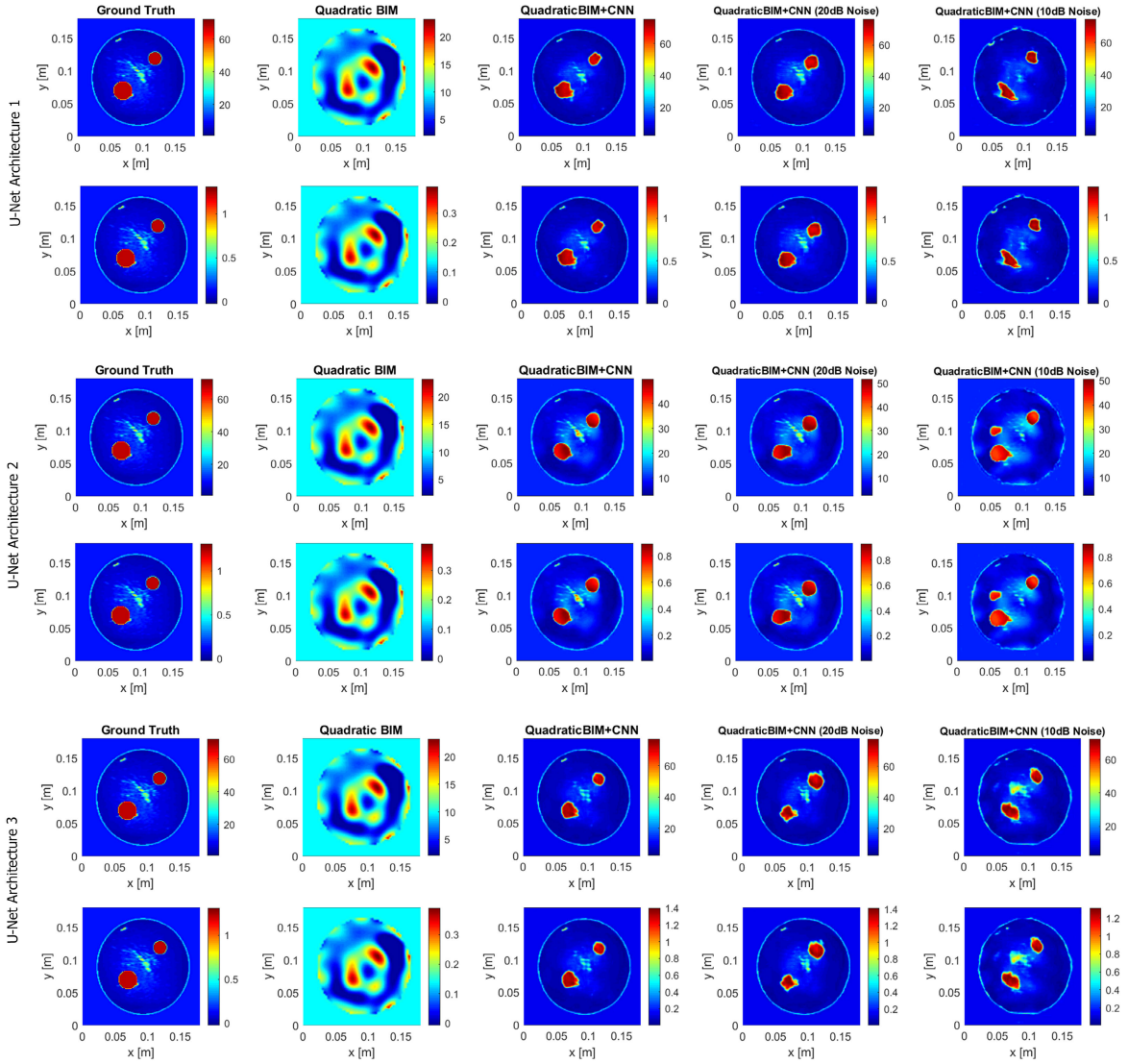

FIGURE 8. **Results obtained for the three U-Net architectures - example of class 2 breast phantom: permittivity (upper) and conductivity (lower).**

the reconstruction quality of the estimated and true images are compared, through a quantitative evaluation of the proposed approach, using the following metrics: Percentage Reconstruction Relative Error R_e (see (4)), Root Mean Square Error *(RMSE)* (see (5)) and the Coefficient of Determination R^2 (see (6)).

$$R_e = \frac{1}{N_p} \sum_{n=1}^{N_p} \left[\frac{\left| \varepsilon^r_{r(n)} - \varepsilon^t_{r(n)} \right|}{\varepsilon^t_{r(n)}} \times 100\% \right] \tag{4}$$

$$RMSE = \sqrt{\frac{\sum_{n=1}^{N_p} \left| \varepsilon^t_{r(n)} - \varepsilon^r_{r(n)} \right|^2}{N_p}} \tag{5}$$

where:

- $\varepsilon^t_{r(n)}$ is the value of the true relative permittivity corresponding to the *n-th* pixel;
- $\varepsilon^r_{r(n)}$ is the value of the reconstructed relative permittivity corresponding to the *n-th* pixel;
- N_p is the total number of pixels.

The coefficient of determination is an essential statistical measure for determining the prediction accuracy of a model by quantifying the difference between the estimated and the actual values. It is represented by the following formula [35], [36]:

$$R^2 = 1 - \frac{SS_{res}}{SS_{tot}} \tag{6}$$

where:

- SS_{res} is the sum of squares of residuals, defined as: $SS_{res} = \sum_{n=1}^{N_p} \{\varepsilon^t_{r(n)} - \varepsilon^r_{r(n)}\}^2$.
- SS_{tot} is the total sum of squares, defined as: $SS_{tot} = \sum_{n=1}^{N_p} \{\varepsilon^t_{r(n)} - \bar{y}\}^2$, where $\bar{y} = \sum_{n=1}^{N_p} \varepsilon^t_{r(n)}/N_p$.

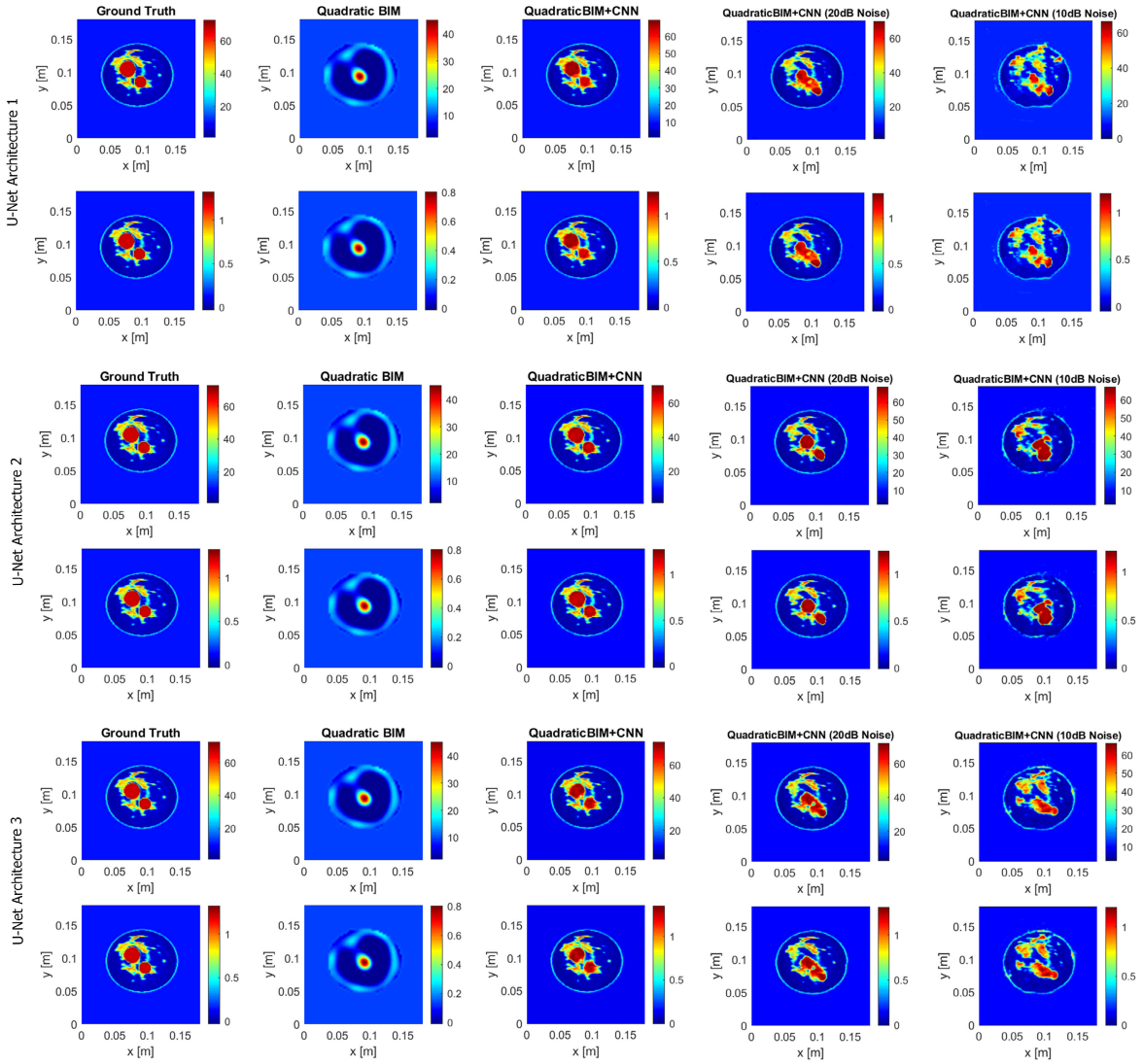

FIGURE 9. Results obtained for the three U-Net architectures - example of Class 3 breast phantom: permittivity (upper) and conductivity (lower).

Typically, the coefficient R^2 falls in the range [0, 1]. However, in some cases it can assume values lying outside this range [35]. These undesired cases indicate an incorrect fitting, which must be carefully managed.

In the context of tumor segmentation, the Intersection Over Union (IoU) [37] is employed, which is responsible for calculating the overlap between the predicted and actual tumor regions. It leads to quantify how accurately the model can segment the tumor. The Intersection over Union (IoU) metric is bounded between 0 and 1. A score of 1 denotes a complete match between the predicted and the ground truth masks, while 0 score indicates no overlap between them. Mathematically, it is expressed as:

$$IoU = \frac{|T \cap P|}{|T \cup P|} \tag{7}$$

where T represents the ground truth mask, while P gives the predicted mask.

The metrics adopted to evaluate the error of breast reconstructions using quadratic BIM only are shown in Table 1. The outcomes of combining quadratic BIM with CNN and the different levels of added noise are also displayed in Table 1. A number of 60 images from the test set and the three types of U-Net architectures are included. In all cases, the proposed method based on the combination of quadratic BIM with CNN greatly outperforms the BIM-only model, by a significant margin. However, measurements of scattered fields in the real environment will be impacted by noise. To further evaluate the effectiveness of the suggested method in a real noisy environment, a 10 dB and 20 dB of white Gaussian noise is added to the scattered electric field measurement. Specifically, an example is considered for each class of breast

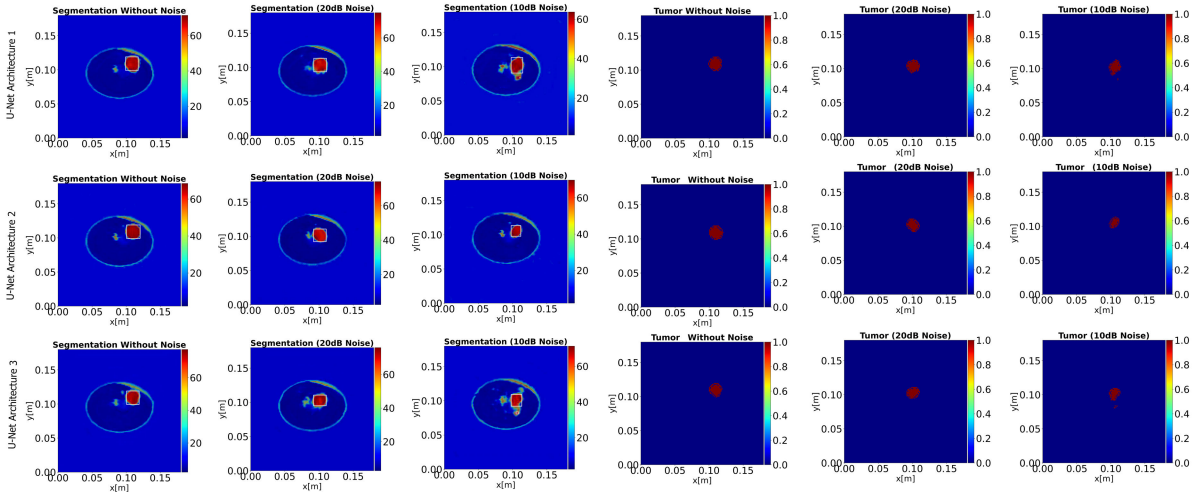

FIGURE 10. Tumor segmentation - Results obtained for the three U-Net architectures - Example of Class 1 breast model.

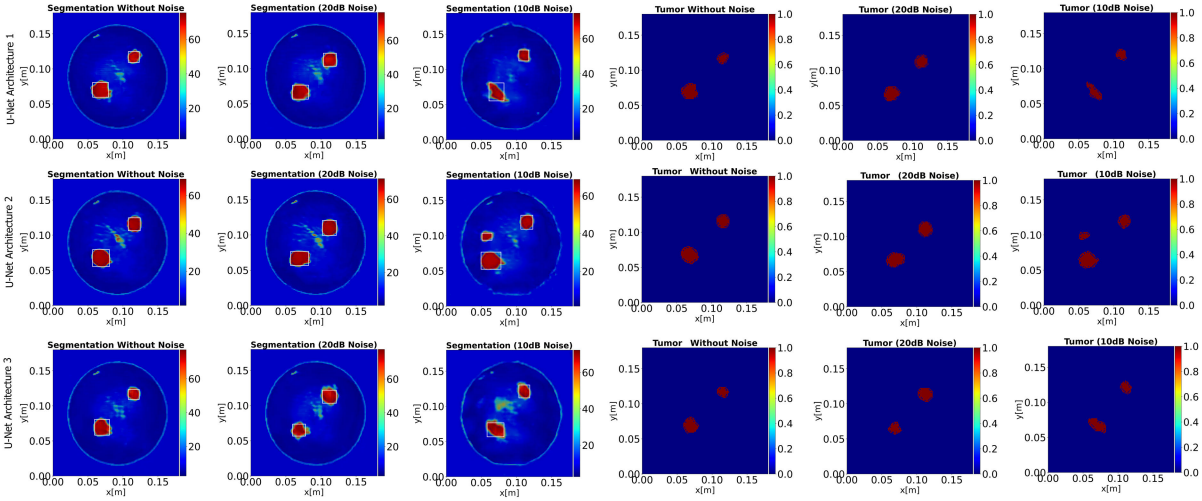

FIGURE 11. Tumor segmentation - Results obtained for the three U-Net architectures - Example of Class 2 breast model.

phantom, and it is tested with the three proposed U-Net architectures. The results of the relative distribution of permittivity and conductivity for the reconstructed breast models (with and without noise), corresponding to Class 1, Class 2 and Class 3, are shown in Fig. 7, Fig. 8 and Fig. 9, respectively.

In the reconstructions with and without noise, U-Net 2 has the lowest mean relative error with 4.04% (no noise), 14.54% (10 dB noise) and 7.21% (20 dB noise), followed by U-Net 1 with a mean relative error of 4.61% (no noise), 17% (10 dB noise) and 7.26% (20 dB noise). U-Net 3 has the highest relative error with 5.60% (noise), 18.77% (10dB noise) and 8.34% (20dB noise).

On the other hand, the fusion of U-Net and Resnet frameworks in tumor segmentation exploits the strengths of both models, resulting into enhanced efficiency and robustness. Table 2 displays the results of the IoU metric used to evaluate the segmentation performance of the three breast models (with and without noise) at the output of each U-Net architecture initially used for reconstruction (U-Net 1, U-Net 2 and U-Net 3). The proposed segmentation method demonstrates to be effective in capturing intricate details and nuanced characteristics of tumors, thereby producing segmentation outcomes with a mean IoU score of 0.995, 0.996 and 0.994 for U-Net 1, U-Net 2 and U-Net 3, respectively, in noise-free environments. For environments with a noise of 10 dB, a mean IoU of 0.979, 0.976 and 0.978 has been obtained for U-Net 1, U-Net 2 and U-Net 3, respectively. Finally, for environments with a noise of 20 dB, a mean IoU of 0.989, 0.989 and 0.988 has been obtained for U-Net 1, U-Net 2 and U-Net 3, respectively.

Although reconstruction and segmentation of breast tissue produce favorable outcomes for non-dense tissues

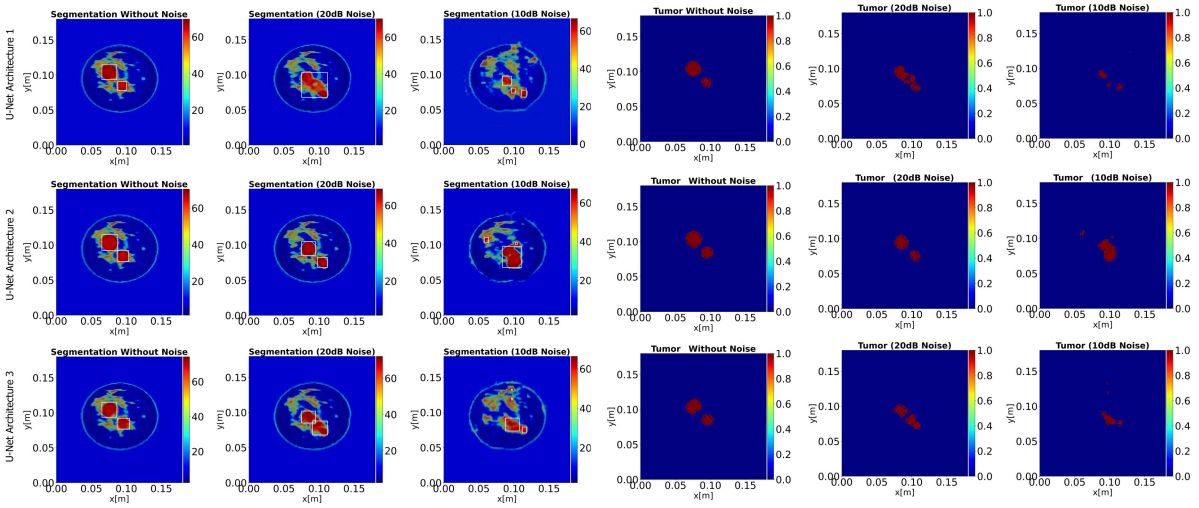

FIGURE 12. Tumor segmentation - Results obtained for the three U-Net architectures - Example of Class 3 breast model.

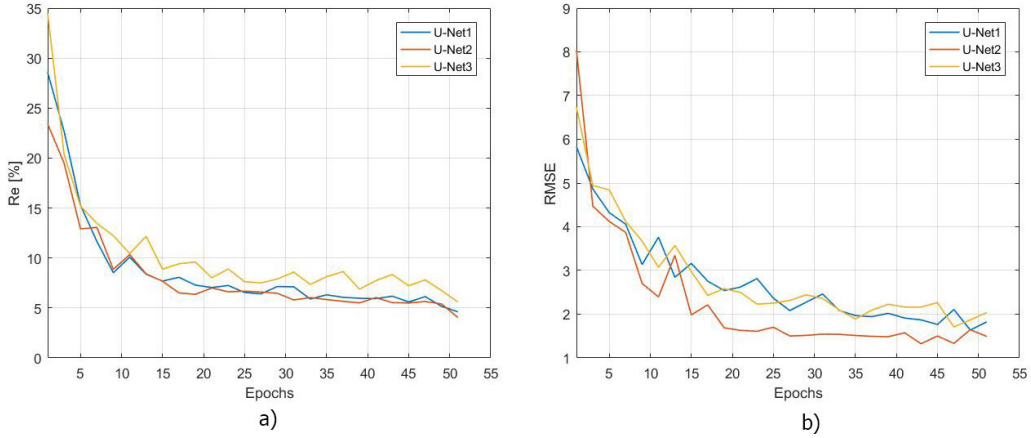

FIGURE 13. Evaluation metrics in image reconstruction and their variation in accordance with the number of network training epochs: a) Relative Error R_e and b) Root Mean Square Error (RMSE).

TABLE 2. Results obtained in the evaluation of tumor segmentation.

		mean IoU		
		Free Noise	10dB Noise	20dB Noise
U-Net1	Class1	0.995	0.984	0.993
	Class2	0.993	0.972	0.988
	Class3	0.996	0.981	0.987
	Mean	**0.995**	**0.979**	**0.989**
U-Net2	Class1	0.996	0.983	0.992
	Class2	0.994	0.967	0.986
	Class3	0.998	0.978	0.988
	Mean	**0.996**	**0.976**	**0.989**
U-Net3	Class1	0.995	0.982	0.991
	Class2	0.992	0.972	0.986
	Class3	0.995	0.981	0.987
	Mean	**0.994**	**0.978**	**0.988**

(classes 1 and 2), they may have limitations when dealing with dense or more complex tissues (class 3). The aforementioned limitations are particularly evident when reconstructed images or segmented tumor regions are exposed to challenging circumstances, such as the introduction of noise. The outcomes of tumor segmentation, in the presence and absence of noise, for the instances reconstructed by U-Net 1, U-Net 2, and U-Net 3 are depicted in Fig. 10, Fig. 11, and Fig. 12, respectively. The presence of dense or complex breast tissue presents difficulties due to its heterogeneous nature, overlapping structures, and increased image disturbance. In some cases, these factors may prevent the accurate identification and segmentation of tumors. For instance, the model may fail to distinguish between tumor regions and the dense tissue surrounding them. This is observed with a higher incidence in the class 3 breast model, in the presence of 10 dB and 20 dB noise.

In contrast, the parameters listed in Table 3 are considered for the networks training, for both the reconstruction and segmentation tasks, in terms of computational costs. Regarding the reconstruction of dielectric profiles, the three distinct

TABLE 3. Model parameterization.

	Reconstruction			Segmentation
Optimized performance measure	**U-Net 1**	**U-Net 2**	**U-Net 3**	**U-Net+ Resnet18**
Filters	128	64	64	64
Convolutional layers	3	4	3	5
Optimizer	SGD	SGD	SGD	Adam
Learning Rate	3.1623e-6	3.1623e-6	3.1623e-6	3e-4
Weight Decay	1e-6	1e-6	1e-6	0
Epochs	51	51	51	40
Time required for training	36h55	17hours	14hours	13minutes
Time required for testing	5s	5s	5s	3s

architectures, namely U-Net 1, U-Net 2, and U-Net 3, are trained. The training process involves a total of 51 epochs, with each epoch lasting 43, 20, and 16 minutes, respectively.

Conversely, the U-net+ResNet backbone architecture is trained to perform the tumor segmentation, by using 40 epochs with a duration of 20 seconds per epoch. The utilization of pre-trained ResNet weights as network initializations results into an accelerated convergence during training and a notable decrease in the computational cost.

Once the networks are trained, it took only 5 seconds to recreate experiments conducted with models independent of the training dataset. All trainings are conducted on a computer with 16 GB of RAM, an AMD Ryzen 7 5800 H processor, Radeon Graphics at 3.20 GHz, and an NVIDIA RTX 3060 graphics card.

Fig. 13 illustrates the Relative Error R_e and RMSE in the evaluation of the reconstruction of breast dielectric profiles, while the coefficient of determination R^2 is shown in Fig. 14, for the test dataset. It can be seen that, as the number of training epochs for each network increases, the R_e and the *RMSE* both decrease. In contrast, as the number of epochs increases, the coefficient of determination approaches 1. This indicates that the dielectric profiles estimated by the three proposed network models closely correspond to the ground truth profiles. The IoU index and loss function curve for breast tumor segmentation during the U-Net+Resnet backbone network training epochs are depicted in Figure 15. The analysis of the (IoU) metric over the course of both training and testing indicates a significant improvement in performance from the initial epochs, with the maximum level of performance being achieved at epoch 40. Furthermore, the reduction in loss exhibits a gradual trend over the course of the training process, indicating that the neural network has effectively optimized its parameters to minimize the disparity between its predictions and the actual labels.

IV. CONCLUSION

Inverse electromagnetic scattering for breast imaging is a typical example of high contrast inversion, and the

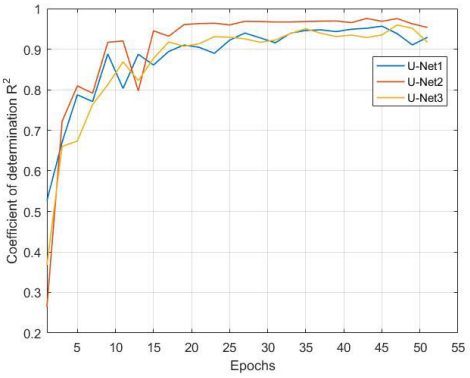

FIGURE 14. Coefficient of Determination R^2 utilized in the assessment of image reconstruction.

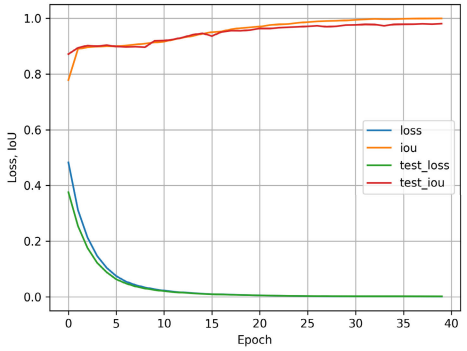

FIGURE 15. U-Net+Resnet18, training results for tumor segmentation: loss function and *IoU*.

implementation required to achieve a high resolution can impose very high computational cost. To solve this inverse problem, while guaranteeing and increasing the accuracy of breast image reconstruction obtained from the quadratic BIM method, three CNN configurations based on the U-Net architecture have been explored and compared in this work, starting from a basic configuration presented in our recent preliminary works. Furthermore, after the breast profile reconstruction, a segmentation procedure is implemented to detect and remark the boundaries of the tumors present in the breast tissue. This process employs a novel architecture which integrates U-Net and Resnet18 to exploit the residual connections of ResNet-18 and its pretrained weights, thus resulting into accurate segmentations at a lower expense. Using a collection of 1500 breast images with tumors in random places, training and validation samples for each proposed network have been generated. To analyze and validate the performance, sixty images distinct from the training set have been employed, considering first images without noise, and then images with added Gaussian noise. In addition, a detailed comparison in terms of computing costs and image reconstruction precision has been conducted, with the aim to perform the lower computational cost, while guaranteeing the convergence to an accurate solution, even in the presence of strong scatterers, thus leading the machine learning procedure

to work as a regularization process overcoming the induced non-linearity. Numerical tests performed in noisy as well as noise-free environments have demonstrated that the proposed method can effectively reconstruct the distribution of the dielectric properties for the breast, with a very good ability to detect abnormal scatterers such as tumors. Nevertheless, some critical issues have been identified in relation to the breast model of class 3 and a noise level of 10 dB, where both the complexity and high density of the model may prevent an accurate reconstruction. Further studies will be performed to face and hopefully overcome the above aspects.

In terms of computational costs, the U-Net 2 and U-Net 3 architectures have revealed the fastest computing speeds, thus demonstrating the strong enhancement as compared to the initial architecture by the same authors. Additional studies are being currently developed to explore innovative CNNs with improved performance in terms of training and testing times.

REFERENCES

[1] T. Deisboeck and J. Y. Kresh, "Biological scaling and physiological time: Biomedical applications," in *Complex Systems Science in Biomedicine*. New York, NY, USA: Springer, 2006, ch. 3.

[2] R. Chen, Z. Wei, and X. Chen, "Three dimensional through-wall imaging: Inverse scattering problems with an inhomogeneous background medium," in *Proc. IEEE 4th Asia–Pacific Conf. Antennas Propag. (APCAP)*, Bali, Indonesia, Jun. 2015, pp. 505–506, doi: 10.1109/APCAP.2015.7374465.

[3] H. Kagiwada, R. Kalaba, S. Timko, and S. Ueno, "Associate memories for system identification: Inverse problems in remote sensing," *Math. Comput. Model.*, vol. 14, pp. 200–202, Jan. 1990.

[4] R. Persico, "Introduction to GPR prospecting," in *Introduction to Ground Penetrating Radar: Inverse Scattering and Data Processing*. Hoboken, NJ, USA: Wiley, 2014, ch. 1.

[5] X. Chen, "Reconstructing dielectric scatterers," in *Computational Methods for Electromagnetic Inverse Scattering*. Hoboken, NJ, USA: Wiley, 2018, ch. 6.

[6] F. Gao, B. D. Van Veen, and S. C. Hagness, "Sensitivity of the distorted born iterative method to the initial guess in microwave breast imaging," *IEEE Trans. Antennas Propag.*, vol. 63, no. 8, pp. 3540–3547, Aug. 2015, doi: 10.1109/TAP.2015.2436406.

[7] P. M. V. D. Berg, A. L. V. Broekhoven, and A. Abubakar, "Extended contrast source inversion," *Inverse Problems*, vol. 15, no. 5, pp. 1325–1344, Oct. 1999.

[8] P. M. V. D. Berg and R. E. Kleinman, "A contrast source inversion method," *Inverse Problems*, vol. 13, no. 6, pp. 1607–1620, Dec. 1997.

[9] X. Chen, "Subspace-based optimization method for solving inverse-scattering problems," *IEEE Trans. Geosci. Remote Sens.*, vol. 48, no. 1, pp. 42–49, Jan. 2010, doi: 10.1109/TGRS.2009.2025122.

[10] Z. Wei and X. Chen, "Deep-learning schemes for full-wave nonlinear inverse scattering problems," *IEEE Trans. Geosci. Remote Sens.*, vol. 57, no. 4, pp. 1849–1860, Apr. 2019, doi: 10.1109/TGRS.2018.2869221.

[11] H. Zhang, Y. Chen, T. J. Cui, F. L. Teixeira, and L. Li, "Probabilistic deep learning solutions to electromagnetic inverse scattering problems using conditional renormalization group flow," *IEEE Trans. Microw. Theory Techn.*, vol. 70, no. 11, pp. 4955–4965, Nov. 2022.

[12] M. T. McCann, K. H. Jin, and M. Unser, "Convolutional neural networks for inverse problems in imaging: A review," *IEEE Signal Process. Mag.*, vol. 34, no. 6, pp. 85–95, Nov. 2017.

[13] Y. LeCun, Y. Bengio, and G. Hinton, "Deep learning," *Nature*, vol. 521, no. 7553, pp. 436–444, 2015.

[14] Y. S. Han, J. Yoo, and J. C. Ye, "Deep residual learning for compressed sensing CT reconstruction via persistent homology analysis," Nov. 2016, *arXiv:1611.06391*. Accessed: Jan. 19, 2023.

[15] K. H. Jin, M. T. McCann, E. Froustey, and M. Unser, "Deep convolutional neural network for inverse problems in imaging," *IEEE Trans. Image Process.*, vol. 26, no. 9, pp. 4509–4522, Sep. 2017.

[16] P. C. Tripathi and S. Bag, "CNN-DMRI: A convolutional neural network for denoising of magnetic resonance images," *Pattern Recognit. Lett.*, vol. 135, pp. 57–63, Jul. 2020.

[17] G. Chen, P. Shah, J. Stang, and M. Moghaddam, "Learning-assisted multimodality dielectric imaging," *IEEE Trans. Antennas Propag.*, vol. 68, no. 3, pp. 2356–2369, Mar. 2020, doi: 10.1109/TAP.2019.2948565.

[18] L. Li, L. G. Wang, F. L. Teixeira, C. Liu, A. Nehorai, and T. J. Cui, "DeepNIS: Deep neural network for nonlinear electromagnetic inverse scattering," *IEEE Trans. Antennas Propag.*, vol. 67, no. 3, pp. 1819–1825, Mar. 2019, doi: 10.1109/TAP.2018.2885437.

[19] O. Ronneberger, P. Fischer, and T. Brox, "U-Net: Convolutional networks for biomedical image segmentation," in *Proc. Int. Conf. Med. Image Comput. Comput.-Assist. Intervent.* Munich, Germany: Springer, 2015, pp. 234–241.

[20] J. Long, E. Shelhamer, and T. Darrell, "Fully convolutional networks for semantic segmentation," in *Proc. IEEE Conf. Comput. Vis. Pattern Recognit. (CVPR)*, Jun. 2015, pp. 3431–3440.

[21] Y. Lecun, L. Bottou, Y. Bengio, and P. Haffner, "Gradient-based learning applied to document recognition," *Proc. IEEE*, vol. 86, no. 11, pp. 2278–2324, Nov. 1998.

[22] A. Krizhevsky, I. Sutskever, and G. E. Hinton, "ImageNet classification with deep convolutional neural networks," *Commun. ACM*, vol. 60, no. 6, pp. 84–90, May 2017.

[23] K. He, X. Zhang, S. Ren, and J. Sun, "Deep residual learning for image recognition," in *Proc. IEEE Conf. Comput. Vis. Pattern Recognit. (CVPR)*, Jun. 2016, pp. 770–778.

[24] M. Mardani, H. Monajemi, V. Papyan, S. Vasanawala, D. Donoho, and J. Pauly, "Recurrent generative adversarial networks for proximal learning and automated compressive image recovery," Nov. 2017, *arXiv:1711.10046*. Accessed: Jan. 19, 2023.

[25] P. Putzky and M. Welling, "Recurrent inference machines for solving inverse problems," Jun. 2017, *arXiv:1706.04008*. Accessed: Jan. 19, 2023.

[26] S. Costanzo, A. Flores, and G. Buonanno, "Machine learning approach to quadratic programming-based microwave imaging for breast cancer detection," *Sensors*, vol. 22, no. 11, p. 4122, May 2022, doi: 10.3390/s22114122.

[27] S. Costanzo and A. Flores, "Enhanced machine learning approach for accurate and fast resolution of inverse scattering problem in breast cancer detection," *Electronics*, vol. 11, no. 15, p. 2308, Jul. 2022.

[28] S. Costanzo, A. Flores, and G. Buonanno, "Machine learning methods for microwave imaging in cancer detection," in *Proc. IEEE Int. Conf. Dependable, Autonomic Secure Comput., Int. Conf. Pervasive Intell. Comput., Int. Conf. Cloud Big Data Comput., Int. Conf. Cyber Sci. Technol. Congr. (DASC/PiCom/CBDCom/CyberSciTech)*, Sep. 2022, pp. 1–5.

[29] M. J. Burfeindt, T. J. Colgan, R. O. Mays, J. D. Shea, N. Behdad, B. D. Van Veen, and S. C. Hagness, "MRI-derived 3-D-printed breast phantom for microwave breast imaging validation," *IEEE Antennas Wireless Propag. Lett.*, vol. 11, pp. 1610–1613, 2012.

[30] A. C. Batista, L. S. Batista, and R. Adriano, "A quadratic programming approach for microwave imaging," *IEEE Trans. Antennas Propag.*, vol. 69, no. 8, pp. 4923–4934, Aug. 2021.

[31] D. S. Jones, *Acoustic and Electromagnetic Waves*. London, U.K.: Oxford Univ. Press, 1986.

[32] M. Siam, M. Gamal, M. Abdel-Razek, S. Yogamani, and M. Jagersand, "RTSeg: Real-time semantic segmentation comparative study," in *Proc. 25th IEEE Int. Conf. Image Process. (ICIP)*, Athens, Greece, Oct. 2018, pp. 1603–1607, doi: 10.1109/ICIP.2018.8451495.

[33] A. Ebrahimi, S. Luo, and R. Chiong, "Introducing transfer learning to 3D ResNet-18 for Alzheimer's disease detection on MRI images," in *Proc. 35th Int. Conf. Image Vis. Comput. New Zealand (IVCNZ)*, Wellington, New Zealand, Nov. 2020, pp. 1–6, doi: 10.1109/IVCNZ51579.2020.9290616.

[34] Z. Kuang and X. Tie, "Flow-based video segmentation for human head and shoulders," 2011, *arXiv:2104.09752*.

[35] T. O. Kvalseth, "Cautionary note about R^2," *Amer. Statistician*, vol. 39, no. 4, pp. 279–285, 1985.

[36] D. Chicco, M. J. Warrens, and G. Jurman, "The coefficient of determination R-squared is more informative than SMAPE, MAE, MAPE, MSE and RMSE in regression analysis evaluation," *PeerJ Comput. Sci.*, vol. 7, p. e623, Jul. 2021, doi: 10.7717/peerj-cs.623.

[37] M. Rahman and Y. Wang, "Optimizing intersection-over-union in deep neural networks for image segmentation," in *Proc. Int. Symp. Vis. Comput.* Cham, Switzerland: Springer, 2016, pp. 234–244.

SANDRA COSTANZO (Senior Member, IEEE) received the Laurea degree (summa cum laude) in computer engineering from Universitã della Calabria, Italy, in 1996, and the Ph.D. degree in electronic engineering from Universitã Mediterranea di Reggio Calabria, Italy, in 2000. Since 2019, she has been an Associate Professor with IREA-CNR (Naples). She is currently an Associate Professor with Universitã della Calabria, where she is the Coordinator of the master's degree in telecommunication engineering and the Rector's Delegate for health safety. She teaches courses on electromagnetic wave propagation, antennas, remote sensing, radar, sensors, and electromagnetic diagnostics. She has authored or coauthored more than 200 contributions to international journals, books, and conferences. Her current research interests include near-field/far-field techniques, antenna measurement techniques, antenna analysis and synthesis, numerical methods in electromagnetics, millimeter wave antennas, reflectarrays, synthesis methods for microwave structures, electromagnetic characterization of materials, biomedical applications, and radar technologies. She is a member of the IEEE MTT-28 Biological Effects and Medical Applications Committee, IEEE Women in Engineering Italy Section, IEEE South Italy Geoscience and Remote Sensing Chapter, Consorzio Nazionale Interuniversitario per le Telecomunicazioni (CNIT), Societã Italiana di Elettromagnetismo (SIEM), and Centro Interuniversitario sulle Interazioni fra Campi Elettromagnetici e Biosistemi (ICEMB). She is a Board Member of the IEEE AP/ED/MTT North Italy Chapter. She received the Telecom Prize for the Best Laurea Thesis, in 1996, and the 2013 Best Academia and Research Application in Aerospace and Defense Award for the application of software-defined radar using the NI USRP 2920 platform. In 2017, she was awarded the Italian National Scientific Qualification for the Full Professor position. She is an Associate Editor of IEEE ACCESS, IEEE JOURNAL OF ELECTROMAGNETICS, RF AND MICROWAVES IN MEDICINE AND BIOLOGY, and *Electronics* (section ''Microwave and Wireless Communications''). She is an Editorial Board Member of *Radioengineering* and *International Journal of RF and Microwave Computer-Aided Engineering*. She is an Editor of the books *Microwave Materials Characterization* (INTECH, 2012) and *Wave Propagation Concepts for Near-Future Telecommunication Systems* (INTECH, 2017). She was the Lead Editor of the Special Issues on *Reflectarray Antennas: Analysis and Synthesis Techniques*, in 2012, *Advances in Radar Technologies*, in 2013, *Compressed Sensing: Applications in Radar and Communications*, in 2016, *Bioengineering Applications of Electromagnetic Wave Propagation*, in 2019, and *Microwave Sensors for Biomedical Applications*, in 2020.

ALEXANDRA FLORES (Student Member, IEEE) was born in Ambato, Ecuador, in 1993. She received the B.S. degree in electronics, telecommunications and networks engineering from Escuela Superior Politécnica de Chimborazo (ESPOCH), Ecuador, in 2017, and the M.S. degree in telecommunications engineering from the University of Calabria, Italy, in 2020, where she is currently pursuing the Ph.D. degree in information and communication technologies. Her current research interests include electromagnetic sensors, microwave image processing, inverse scattering, machine learning, and biomedical applications. She is an IEEE Women in Engineering Member.

GIOVANNI BUONANNO (Member, IEEE) received the M.S. degree (summa cum laude) in electronic engineering from Seconda Universitã degli Studi di Napoli (SUN), Aversa, Italy, in 2014, and the Ph.D. degree in industrial and information engineering from the University of Campania, in 2018. Then, he joined the Research Group in Applied Electromagnetics, SUN. He defended his Ph.D. thesis, in January 2019. He is currently a Research Fellow with the University of Calabria. His current research interests include the analysis and design of non-uniformly-spaced antenna arrays, biomedical applications, signal processing, and machine learning.

Open Access funding provided by 'Università della Calabria' within the CRUI CARE Agreement